# Dynamics Study of the $O_2(v) + HO_2$ Atmospheric Reaction

**Lei Zhang and António J. C. Varandas*,†**

*Departamento de Química, Universidade de Coimbra, P-3049 Coimbra Codex, Portugal*

*Received: July 10, 2001; In Final Form: September 17, 2001*

A quasiclassical trajectory study of the title five-atom reaction is reported for vibrational states of $O_2$ over the range of $12 \leq v \leq 27$ using a realistic double many body expansion potential energy surface recently reported for $HO_4(^2A)$. The results indicate that it can be a potential source of ozone in the upper atmosphere.

## 1. Introduction

Vibrationally excited molecules can play a significant role in chemical reactions due to their unique and interesting chemical and physical properties. Examples of common and naturally occurring processes that lead to the formation of vibrationally excited molecules are exothermic chemical reactions, ultraviolet photodissociation, and electrical discharges. In fact, with the further development of stimulated emission pumping[1−9] and overtone pumping,[10−17] investigation of collisional properties of vibrationally hot molecules has blossomed. Moreover, for vibrationally excited diatomic species, fully quantum-state-resolved experiments are possible and quantum mechanical identification of all excited states is unambiguous. The vibrational dependence of the collision dynamics involving diatomics is therefore an intriguing topic since it offers an understandable bridge between low and high vibrational excitation.[18]

Vibrationally excited molecular oxygen (hereafter denoted by $O_2(v)$) can be formed with significant efficiency in the photodissociation of $O_3$ at[19] 248 and[20] 226 nm in states as high as $v = 27$. This vibrationally excited $O_2(^3\Sigma_g^-)$ has recently been proposed[6,20−22] to explain the limitations of atmospheric ozone models.[23−25] Indeed, although questionable,[26] there has been a long-standing problem with ozone models for the upper stratosphere and mesosphere that underpredict the measured ozone concentrations,[25] with the above unexpected ozone source being viewed as a possible explanation for the discrepancy. Such an "ozone deficit" problem has also prompted much effort to identify new sources of ozone.[6,27−34]

Once produced, highly vibrationally excited species either fluoresce or undergo deactivation in collisions with ambient molecules such as $O_2$, $O_3$, OH, $N_2$, $CO_2$, and $N_2O$. Over the past decade, both experimental and theoretical progress has been made in measuring the vibrational level dependence of the total removal rate constants in collisional processes.[6,18,19,21,27,28,30−36] However, remarkably absent from this progress list is $HO_2$, which is an important natural species of the atmosphere. In fact, the $HO_2$ radical is a key intermediate for many chemical reactions such as those involved in atmospheric chemistry,[37−44] stratospheric formation and destruction of ozone,[45−47] and photochemical air pollution.[48−52] An investigation of the collisional properties of highly vibrationally excited $O_2$ with $HO_2$ radicals is therefore of great interest.

Until recently, no single theoretical study of the $O_2(v) + HO_2$ reaction had been reported in the literature. Such a lack of theoretical work can only be attributed to difficulties in calculating a reliable $HO_4(^2A)$ potential energy surface. On the basis of previous work,[53−58] we have developed[59] such a realistic surface by using the double many body expansion[60,61] (DMBE) method as implemented for single-valued functions. Moreover, we have used[59,62,63] this $HO_4$ DMBE surface to study the reaction $OH(v) + O_3 \rightarrow HO_2 + O_2$. For the states $v = 0$ and 9, good agreement has been found with the data recommended by the IUPAC subcommittee on gas kinetics data evaluation for atmospheric chemistry[64] and the measurements of Greenblatt and Wiesenfeld,[65] respectively. In turn, for $1 \leq v \leq 8$, there is essentially no experimental data, and hence a comparison with available results on the $OH(v)$ quenching based on nonreactive collisions has been presented. The results indicate that vibrational excitation strongly enhances reactivity, with removal of vibrationally excited OH occurring predominantly through chemical reaction. Thus, such a work paved the way to investigate the dynamics and kinetics of the $O_2(v) + HO_2$ reaction for high $v$ states that as shown below, may be a potential source of ozone in the upper atmosphere.

A major goal of the present work is to report a detailed study of the reaction

$$O_2(v = 12-27) + HO_2 \rightarrow O_3^*/O_3 + OH \qquad (1)$$

where the star indicates that the formed ozone molecules have an internal energy above the dissociation limit. Thus, they will ultimately decompose through the unimolecular dissociation reaction

$$O_3^* \rightarrow O_2 + O \qquad (2)$$

or will stabilize in the presence of some inert species (M) through the reaction

$$O_3^* + M \rightarrow O_3 + M \qquad (3)$$

For the dynamics calculations, we will employ (as in previous work[59,62,63]) the quasiclassical trajectory (QCT) method and the $HO_4(^2A)$ DMBE potential energy surface; throughout the paper, the absence of a specific vibrational state in a reactant species implies that it is in the ground vibrational state (e.g., $HO_2 \equiv HO_2(v_1 = 0, v_2 = 0, v_3 = 0)$, where $v_1$ is the quantum number for the symmetric stretching vibrational normal mode, $v_2$ is for the bending normal mode, and $v_3$ is for the asymmetric stretching normal mode). The paper is organized as follows. Section 2 provides a brief survey of the $HO_4(^2A)$ DMBE

† Corresponding author e-mail: varandas@qtvs1.qui.uc.pt.

10.1021/jp0126309 CCC: $20.00 
Published on Web 10/24/2001

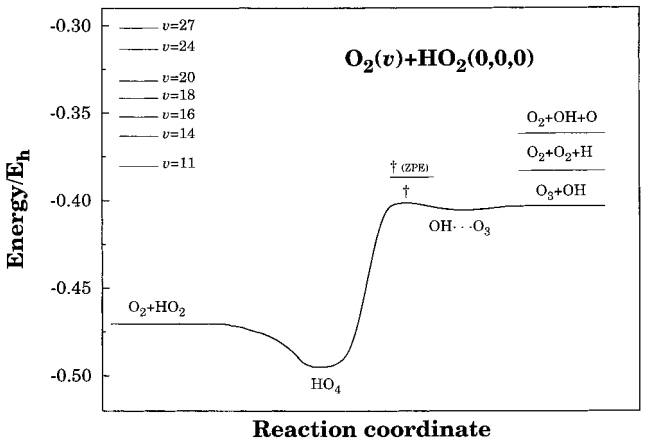


**Figure 1.** Minimum energy path for formation of $O_3^*/O_3 + OH$. The saddle point geometry is indicated by the symbol †. Also shown are the energies of $O_2$ ($v = 11 - 27$) + $HO_2$, $O_2 + O_2 + H$, and $O_2 + OH + O$.

potential energy surface, while the computational method is described in section 3. The dynamics results are presented and disscussed in section 4, while the major conclusions are in section 5.

## 2. Potential Energy Surface

All calculations reported in this work have employed a full-dimensional (9D) DMBE potential energy surface[59] for the ground electronic state of $HO_4$. Because its topography has been illustrated elsewhere,[59,62,63] we report in Figure 1 only the minimum energy path for the title reaction and some energetic features that are of relevance for the present work. These refer to the energetics of the $O_2(v = 12-27) + HO_2$ channels and relevant product ones. Note that for $v = 11$, the reactive channel leading to ozone formation is just barely open. However, for vibrational states $v \geq 16$, all reactive channels ($O_3^*/O_3 + OH$, $O_2 + O_2 + H$, and $O_2 + OH + O$) are accessible over the complete range of translational energies.

## 3. Computational Procedures

Following previous work,[59,62,63] we have used the QCT method in the present study of the $O_2(v) + HO_2$ reaction. To run the classical trajectories, we have utilized extensively adapted versions of the MERCURY/VENUS96[66] codes, which accommodate the $HO_4$ DMBE potential energy surface and make the appropriate assignment of the relevant reactive channels described in section 2. Calculations have been carried out for diatom−triatom translational energies over the range of $1.0 \leq E_{tr}/\text{kcal mol}^{-1} \leq 20$, as specified in Table 1. In all cases, the initial rotational quantum number of the colliding $O_2$ molecule has been fixed at the ground level ($j = 1$). Although the most populated rotational level in a Boltzmann distribution at a typical stratospheric temperature of 150 K is $j = 5$, we believe that such a constraint has no major effect on the conclusions to be drawn in the present work. This is tentatively elucidated by carrying out some calculations of the thermal rate coefficient using a thermally averaged $j$ distribution. For this, we have selected the temperatures of $T = 150$ and 300 K, with the latter being chosen to define the rotational distribution of $HO_2$ in all calculations reported in this work when $O_2$ is kept in the $j = 1$ rotational state. In fact, the $HO_2$ molecule has then been considered in the ground vibrational state ($v_1 = 0$, $v_2 = 0$, $v_3 = 0$) with its rotational energy being assigned by using the microcanonical sampling scheme for a temperature of 300 K. As the results reported below seem to indicate, such a choice should not have a drastic influence on the final results. An optimum step size for numerical integration of $1.5 \times 10^{-16}$ s has been chosen, which warrants conservation of the total energy to better than 2 parts in $10^5$. In turn, the diatom−triatom initial separation has been fixed at $17a_0$ (a value sufficiently large to make the interaction negligible), while the maximum value of impact parameter ($b_{max}$) that leads to reaction has been estimated by computing batches of 200 trajectories for fixed values of $b$. This procedure allows an accuracy in $b_{max}$ of $\pm 0.2a_0$ or so. Batches of at least 2000 trajectories have then been carried out for each translational energy making a total of about $8 \times 10^4$ trajectories. Such a number of trajectories is enough to yield reactive cross sections with an error smaller than about 10% for all translational energies considered in the current work.

**TABLE 1: Summary of Trajectory Calculations for $O_3^*/O_3$ + OH Formation**

| $v$ | $E_{tr}$ (kcal mol$^{-1}$) | $b_{max}(a_0)$ | $N_r$[a] | $100P_r$ | $\sigma^r \pm \Delta\sigma^r/a_0^2$ |
|---|---|---|---|---|---|
| 18 | 1.0 | 6.80[b] | 2 | 0.10 | $0.15 \pm 0.11$ |
| | 2.0 | 4.54 | 3 | 0.15 | $0.10 \pm 0.06$ |
| | 4.0 | 3.78 | 4 | 0.20 | $0.09 \pm 0.05$ |
| | 6.0 | 3.40 | 14 | 0.70 | $0.25 \pm 0.07$ |
| | 8.0 | 3.78 | 13 | 0.65 | $0.29 \pm 0.08$ |
| 20 | 1.0 | 9.83 | 9 | 0.45 | $1.37 \pm 0.45$ |
| | 2.0 | 8.31 | 16 | 0.80 | $1.74 \pm 0.43$ |
| | 4.0 | 7.18 | 17 | 0.85 | $1.38 \pm 0.33$ |
| | 6.0 | 6.43 | 20 | 1.00 | $1.30 \pm 0.29$ |
| | 8.0 | 6.80 | 21 | 1.05 | $1.53 \pm 0.33$ |
| | 12.0 | 7.56 | 21 | 1.05 | $1.88 \pm 0.41$ |
| | 16.0 | 7.56 | 28 | 1.40 | $2.51 \pm 0.47$ |
| 24 | 1.0 | 11.72 | 63 | 3.15 | $13.58 \pm 1.68$ |
| | 2.0 | 10.20 | 61 | 3.05 | $9.98 \pm 1.26$ |
| | 4.0 | 9.07 | 58 | 2.90 | $7.50 \pm 0.97$ |
| | 6.0 | 8.50 | 51 | 2.55 | $5.79 \pm 0.80$ |
| | 8.0 | 8.50 | 50 | 2.50 | $5.68 \pm 0.79$ |
| | 12.0 | 8.31 | 55 | 2.75 | $5.97 \pm 0.79$ |
| 27 | 1.0 | 12.09 | 101 | 5.05 | $23.21 \pm 2.25$ |
| | 2.0 | 10.39 | 99 | 4.95 | $16.80 \pm 1.65$ |
| | 4.0 | 9.26 | 97 | 4.85 | $13.06 \pm 1.29$ |
| | 6.0 | 8.88 | 82 | 4.10 | $10.16 \pm 1.10$ |
| | 8.0 | 8.88 | 79 | 3.95 | $9.79 \pm 1.08$ |
| | 12.0 | 8.50 | 70 | 3.50 | $7.95 \pm 0.93$ |

[a] Number of reactive trajectories. [b] For convenience, the data in this and following tables is often reported with two significant figures, although this by no means implies that such an accuracy is always applicable, as it can be anticipated from the number of reactive events.

For a specified translational energy, all relevant reactive cross sections and associated 68% uncertainties have been calculated. They will be denoted $\sigma^x$ and $\Delta\sigma^x$, respectively, with $x$ specifying the outcome $x = r$, total (this stands for formation of $O_3^*/O_3 + OH$, $O_2 + O_2 + H$, and $O_2 + OH + O$). From the cross sections, and assuming a Maxwell−Boltzmann distribution over the translational energy, the specific thermal rate coefficients are obtained as

$$k^x(T) = g_e(T)\left(\frac{2}{k_B T}\right)^{3/2}\left(\frac{1}{\pi\mu}\right)^{1/2}\int_0^\infty E_{tr}\sigma^x \exp\left(-\frac{E_{tr}}{k_B T}\right) dE_{tr} \quad (4)$$

where $g_e(T) = 1/3$ is the electronic degeneracy factor that corresponds to the ratio of the electronic partition functions, $k_B$ is the Boltzmann constant, $\mu$ is the reduced mass of the colliding particles, and $T$ is the temperature.

**TABLE 2: Summary of Trajectory Calculations That Led to Other Products**

| | | $O_2 + O_2 + H$ | | | $O_2 + OH + O$ | | |
|---|---|---|---|---|---|---|---|
| $v$ | $E_{tr}$ (kcal mol−1) | $N_r$ | $100P_r$ | $\sigma^r \pm \Delta\sigma^r/a_0^2$ | $N_r$ | $100P_r$ | $\sigma^r \pm \Delta\sigma^r/a_0^2$ |
| 18 | 1.0 | | | | 2 | 0.10 | 0.15 ± 0.10 |
| | 2.0 | 2 | 0.10 | 0.07 ± 0.05 | 2 | 0.10 | 0.07 ± 0.05 |
| | 4.0 | | | | 3 | 0.15 | 0.07 ± 0.04 |
| | 6.0 | 1 | 0.05 | 0.02 ± 0.02 | 9 | 0.45 | 0.16 ± 0.05 |
| | 8.0 | 1 | 0.05 | 0.02 ± 0.02 | 10 | 0.50 | 0.22 ± 0.07 |
| 20 | 1.0 | 2 | 0.10 | 0.30 ± 0.21 | 19 | 0.95 | 2.88 ± 0.66 |
| | 2.0 | 1 | 0.05 | 0.11 ± 0.11 | 19 | 0.95 | 2.06 ± 0.47 |
| | 4.0 | 2 | 0.10 | 0.16 ± 0.11 | 27 | 1.35 | 2.19 ± 0.42 |
| | 6.0 | 1 | 0.05 | 0.07 ± 0.07 | 34 | 1.70 | 2.20 ± 0.37 |
| | 8.0 | 3 | 0.15 | 0.22 ± 0.13 | 37 | 1.85 | 2.69 ± 0.44 |
| | 12.0 | 2 | 0.10 | 0.18 ± 0.13 | 46 | 2.30 | 4.13 ± 0.60 |
| | 16.0 | 6 | 0.30 | 0.54 ± 0.22 | 65 | 3.25 | 5.83 ± 0.71 |
| 24 | 1.0 | 9 | 0.45 | 1.94 ± 0.65 | 141 | 7.05 | 30.40 ± 2.47 |
| | 2.0 | 3 | 0.15 | 0.49 ± 0.28 | 166 | 8.30 | 27.15 ± 2.02 |
| | 4.0 | 4 | 0.20 | 0.52 ± 0.26 | 174 | 8.70 | 22.49 ± 1.37 |
| | 6.0 | 5 | 0.25 | 0.57 ± 0.25 | 186 | 9.30 | 21.13 ± 1.48 |
| | 8.0 | 5 | 0.25 | 0.57 ± 0.25 | 186 | 9.30 | 21.13 ± 1.48 |
| | 12.0 | 6 | 0.30 | 0.65 ± 0.27 | 210 | 10.50 | 22.81 ± 1.49 |
| 27 | 1.0 | 7 | 0.35 | 1.61 ± 0.61 | 284 | 14.20 | 65.25 ± 3.59 |
| | 2.0 | 7 | 0.35 | 1.19 ± 0.45 | 306 | 15.30 | 51.92 ± 2.73 |
| | 4.0 | 2 | 0.10 | 0.27 ± 0.19 | 326 | 16.30 | 43.91 ± 2.22 |
| | 6.0 | 4 | 0.20 | 0.50 ± 0.25 | 326 | 16.30 | 40.40 ± 2.05 |
| | 8.0 | 4 | 0.20 | 0.50 ± 0.25 | 330 | 16.50 | 40.89 ± 2.06 |
| | 12.0 | 7 | 0.35 | 0.80 ± 0.30 | 391 | 19.55 | 44.41 ± 2.01 |

## 4. Results and Discussion

Tables 1 and 2 summarize the trajectory calculations carried out in the present work. Column one indicates the vibrational quantum number of the $O_2$ radical while the studied translational energies are given in column two. For these initial translational energies, the only open reactive channel for the formation of $O_3^*/O_3 + OH$ is

$$O_aO_b + HO_dO_c \rightarrow O_aO_bO_c + O_dH \quad (5)$$

where the indices *a*, *b*, *c*, and *d* label the four oxygen atoms (no consideration is made of different isomeric species; i.e., $O_cO_aO_b$, $O_aO_cO_b$, and $O_aO_bO_c$ are treated jointly). Clearly, such a reaction refers to the formation of $O_3^*/O_3 + OH$ products via an oxygen atom abstraction mechanism. As mentioned in section 2, there are additional reactive channels leading to $O_2 + O_2 + H$ and $O_2 + OH + O$. For the case of $O_2 + O_2 + H$, the dominant channel is

$$O_aO_b + HO_dO_c \rightarrow O_aO_b + O_cO_d + H \quad (6)$$

In turn, for the products $O_2 + OH + O$, the open reactive channels are

$$O_aO_b + HO_dO_c \rightarrow O_aO_b + O_dH + O_c \quad (7)$$

$$\rightarrow O_aO_c + O_dH + O_b \quad (8)$$

$$\rightarrow O_bO_c + O_dH + O_a \quad (9)$$

In this case, the reactions in eqs 8 and 9 have identical probabilities of occurrence, with any differences being attributable only to statistical errors in the QCT calculations. However, as compared with such reactive channels, the reaction in eq 7 has a small probability. Note that the reactive probabilities for the formation of $O_3^*/O_3 + OH$ and $O_2 + OH + O$ increase with quantum number $v$, while they only slightly increase for the formation of $O_2 + O_2 + H$. In summary, the dominant reactive channels for the title reaction are the formation of $O_3^*/O_3 + OH$ and $O_2 + OH + O$. For high $v$ states, the formation of $O_2 + OH + O$ plays a role even more significant than $O_3^*/O_3 + OH$.

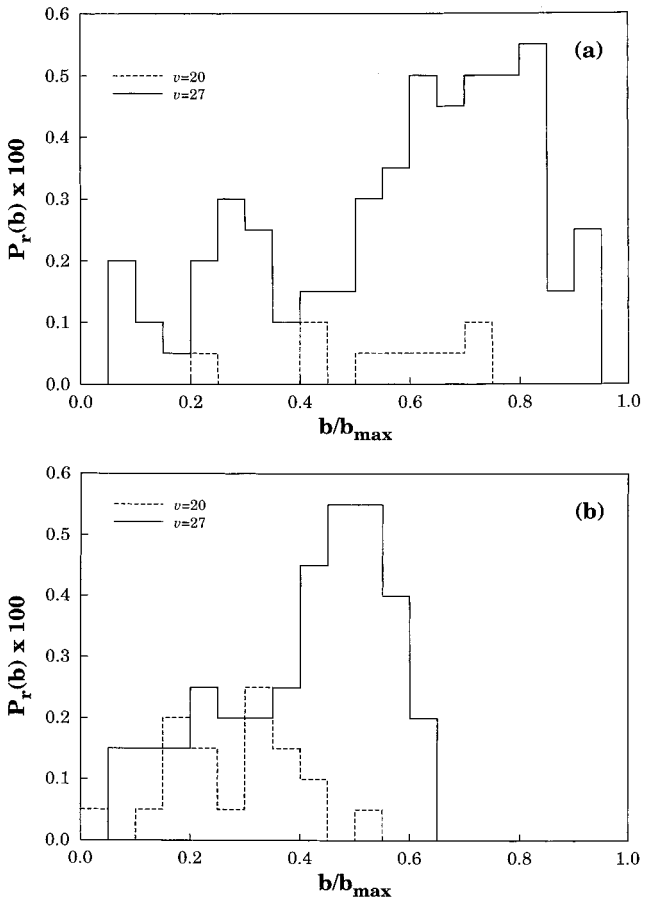


**Figure 2.** Opacity function for the formation of $O_3^*/O_3$: (a) capture type regime, $E_{tr} = 1$ kcal mol$^{-1}$; (b) barrier type regime, $E_{tr} = 12$ kcal mol$^{-1}$.

**4.1. Dynamical Features.** Table 1 shows the dependence of the maximum impact parameter with translational energy for the formation of $O_3^*/O_3 + OH$. As expected, the value of $b_{max}$ increases with decreasing translational energy while for higher translational energies $b_{max}$ is essentially constant or slightly increases with $E_{tr}$. Thus, we expect that reaction may occur via both "capture type" and "barrier type" mechanisms. Such a dependence of $b_{max}$ on $E_{tr}$ may be rationalized as follows. The dominant interactions between $O_2$ and $HO_2$ are, at large distances, of the quadrupole−dipole and quadrupole−quadrupole electrostatic types. Because the $O_2$ molecule is highly vibrationally excited (and this stretching leads to an increase of its electric quadrupole moment), one may then expect a more attractive long-range interaction for favorable orientations. A similar expectation holds for the dispersion forces. Thus, long-range forces may in part explain why $b_{max}$ increases with decreasing translational energy. For high translational energies, such forces play a less important role, with an increase of translational energy leading to a small increase in $b_{max}$.

Figure 2 shows typical opacity functions (i.e., reactive probability vs impact parameter) for low (a) and high (b) translational energies and vibrational quantum numbers $v = 20$ and 27. For clarity, only the cases corresponding to $E_{tr} = 1$ and 12 kcal mol$^{-1}$ are shown in Figure 2. Note that the abcissae in these plots are $b/b_{max}$, with $b_{max}$ being the largest impact parameter found in all batches that were run in the present work ($12.09a_0$). The notable feature in Figure 2 is perhaps the fact that the opacity function shows two different patterns. For high

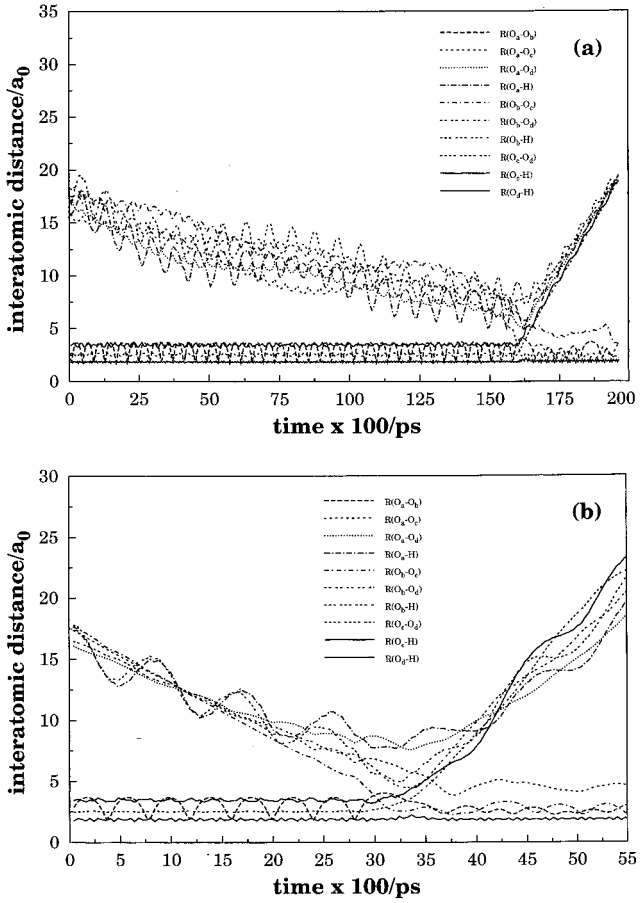


**Figure 3.** Typical distance vs time plots for the title reaction: (a) capture type regime ($v = 27$, $E_{tr} = 1$ kcal mol$^{-1}$); (b) barrier type regime ($v = 27$, $E_{tr} = 12$ kcal mol$^{-1}$).

translational energies, the opacity function has a bell shape (more common for reactions that have a threshold energy), while for low translational energies it increases with impact parameter showing the effect of long-range forces.

Figure 3 shows interatomic distance vs time plots for typical trajectories leading to the formation of $O_3^*/O_3 + OH$ in the capture type and barrier type regimes (these are defined from the shape of the associated excitation function to be discussed later), with examples being given of short-lived and long-lived trajectories. Clearly, on an average sense, long-lived trajectories are more likely to occur in the capture type regime.

Table 3 contains the average values of the scattering angle distribution for $O_2(v)$ and several translational energies. As seen, at moderate and high translational energies, the scattering tends to be backward with increasing vibrational state of molecular oxygen. This suggests a tendency for the products to be formed directly under such conditions. For $v = 18$, we observe from Table 3 that the scattering angle becomes slightly forward with increasing translational energy. It should be recalled that even for this vibrational state, most product ozone molecules are of $O_3^*$ type and hence will dissociate once given enough time to do so (see section 4.3). However, if we consider the lifetime of the formed $O_3/O_3^*$ species, we observe that the scattering angle approximately correlates with the complex lifetime that is found to decrease with translational energy. For example, the average complex lifetime calculated using the method described in ref 63 for $v = 20$ is 0.627 ps at $E_{tr} = 1.0$ kcal mol$^{-1}$ while for $E_{tr} = 12.0$ kcal mol$^{-1}$ one obtains 0.238 ps. For $v = 27$, typical values for the capture type ($E_{tr} = 1.0$ kcal mol$^{-1}$) and barrier type ($E_{tr} = 12.0$ kcal mol$^{-1}$) regimes are 0.442 and 0.148 ps,

**TABLE 3: Average Value of Scattering Angle in Degrees**

| $v$ | $E_{tr}$ (kcal, mol$^{-1}$) | $\langle\Theta_{scatt}\rangle$ |
|---|---|---|
| 18 | 1.0 | 109.6 |
| | 2.0 | 92.7 |
| | 4.0 | 86.5 |
| | 6.0 | 61.7 |
| | 8.0 | 63.4 |
| | | 82.8[a] |
| 20 | 1.0 | 107.3 |
| | 2.0 | 97.3 |
| | 4.0 | 93.2 |
| | 6.0 | 89.1 |
| | 8.0 | 95.9 |
| | 12.0 | 93.8 |
| | 16.0 | 98.0 |
| | | 96.4[a] |
| 24 | 1.0 | 115.6 |
| | 2.0 | 105.4 |
| | 4.0 | 112.1 |
| | 6.0 | 115.0 |
| | 8.0 | 117.4 |
| | 12.0 | 111.5 |
| | 16.0 | 105.2 |
| | | 111.7[a] |
| 27 | 1.0 | 105.5 |
| | 2.0 | 104.4 |
| | 4.0 | 114.6 |
| | 6.0 | 113.0 |
| | 8.0 | 114.0 |
| | 12.0 | 115.2 |
| | 16.0 | 116.5 |
| | | 111.9[a] |

[a] Average scattering angle over the reported translational energies.

respectively. Note that these complex lifetimes should be sufficiently long to allow many oscillations in the vibrational modes of the complex, thus warranting the possibility of internal energy exchange. This result finds support on studies of the decay rate of the energized $O_3^*$ complexes to be reported in section 4.3. Note further that such a tendency for the scattering angle to diminish with translational energy ceases to be observed for high $v$ states. In fact, the scattering angle becomes nearly insensitive to translational energy for vibrational states larger than $v \simeq 24$.

**4.2. Energetic Features.** Figure 4 displays the products energy distribution for the $O_2(v = 27) + HO_2$ reaction at initial translational energies of 1, 6, and 12 kcal mol$^{-1}$. Clearly, the outcoming molecules have a considerable internal energy content, with a significant part of it being in the rotational degrees of freedom; that is, part of the energy of the system has been converted into rotational energy in the products. In fact, a significant fraction of the product $O_3$ molecules has a vibrational energy above the $O_2 + O$ dissociation threshold, which is 26.06 kcal mol$^{-1}$. This result implies that such vibrationally hot ozone ($O_3^*$) molecules will dissociate once given enough time to do so. Thus, such trajectories might also be counted as forming $O_2 + OH + O$. However, because this has no implications on the conclusions to be drawn later, we will count as ozone-forming trajectories those leading to both $O_3 + OH$ and $O_3^* + OH$. Indeed, any dissociating $O_3^*$ species will finally lead again to chemically stable ozone molecules through three-body recombination of the outcoming oxygen atom with molecular oxygen.

The partitioning of the energy release in the product molecules is also exhibited in Table 4. The notable feature is perhaps the fact that the average value of the vibrational energy of the $O_3^*/O_3$ radical represents more than a half of the total energy of

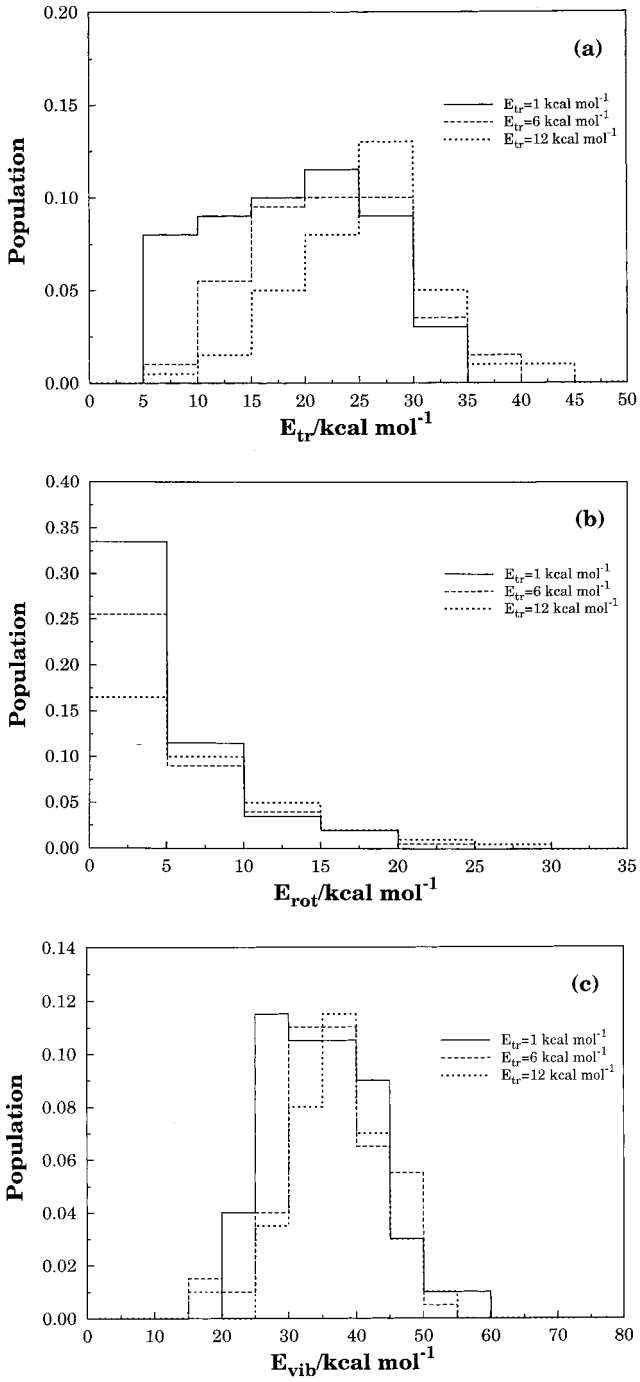


**Figure 4.** Energy distributions in the products for $O_3^*/O_3$ formation ($v = 27$): (a) translational, (b) rotational, and (c) vibrational energy.

the products. Also interesting is the fact that the percent translational energy plays a significant role, representing about 1/3 of the total energy of the products. This may be rationalized by noting that for direct reactions on a repulsive surface, one may expect from Polanyi's rules (the saddle point occurs late in the products valley) that vibrational energy in the reactants can be efficiently converted into translational energy of the products. Note also that the average vibrational energy of the product $O_3^*/O_3$ species is much higher than the corresponding zero-point energy[67] (ZPE) of 4.2 kcal mol$^{-1}$. Thus, for practical purposes, we may safely ignore in the present study the problem of ZPE leakage. Of course, no consideration is being given to the vibrational energy content of the other product molecule; for a detailed discussion of this issue in the context of the OH-($v$) + $O_3$ reaction, see ref 62.

Figure 5 shows the vibrational−rotational distribution of $O_3^*/O_3$ for the $O_2(v = 27) + HO_2$ reaction at two distinct energies (1 and 8 kcal mol$^{-1}$). Despite some scattering, it is possible to assign a relatively narrow range of internal energies to the $O_3^*$ complexes for $E_{tr} = 1$ kcal mol$^{-1}$. The dotted line indicates the threshold energy for the dissociation of $O_3^*$ into $O_2 + O$, while in dash are the lines corresponding to constant averaged internal energies, $\langle E_{vib} + E_{rot} \rangle$. Clearly, in both cases, most points lie above the dissociation threshold, which implies that the dominant product ozone molecules are energized species.

**4.3. Dissociation Reaction $O_3^* \rightarrow O_2 + O$.** We now discuss the dynamics of the energized $O_3^*$ complexes, which carry an internal energy above the threshold for $O_2 + O$ dissociation. For this, once an $O_3^*$ complex has been formed, we have allowed the trajectory to continue until dissociation. Figure 6 shows the logarithm of the decay rate of the $O_3^*$ complexes as a function of time. It is seen that after some induction time, the rate of decay is roughly exponential with the concave curvature possibly being due to the fact that the ensembles of trajectories deviate from genuine microcanonical ones. Such a result suggests a RRKM type behavior, implying that efficient randomization of energy occurs among the various degrees of freedom. Thus, after some induction time, the energy contained in specific vibrational modes is promptly pumped to those modes that are coupled to the reaction path leading to dissociation. Such an observation is similar to that reported elsewhere[27] for the $O_3^*$ complexes formed in the $O_2(v') + O_2(v'')$ reaction.

**4.4. Cross Sections.** We now examine the shape of the excitation function (cross section vs translational energy) with the associated 68% error bars for removal of $O_2(v)$ via reactive collisions (i.e., in processes leading to the formation of $O_3^*/O_3 + OH$, $O_2 + O_2 + H$, and $O_2 + OH + O$), which is shown in Figure 7. (Similar considerations apply to the excitation functions for $O_2(v)$ removal only via the formation of $O_3^*/O_3 + OH$. Because their shapes differ only quantitatively, we show only the total reactive $O_2(v)$ removal in Figure 7.) Clearly, for values of $v$ larger than a given threshold $v_C = 18$, such curves have in general two opposite trends that explain their shapes. At low energies, the capture type regime dominates leading to the well-established[68−70] decreasing dependence of $\sigma^r$ with $E_{tr}$. For high translational energies, one observes instead the common pattern found in reactions that have an energy threshold; that is, $\sigma^r$ is an increasing function of $E_{tr}$. As a result, the excitation function shows a minimum in the region where the two effects balance each other. It is interesting to note that $\sigma^r$ increases slowly at high energies, suggesting that the capture type mechanism dominates over the whole range of translational energies. Such results lead to the conclusion that the high vibrational excitation in $O_2$ effectively promotes the rupture of the OO bond of the $HO_2$ radical while enhancing the role of long-range forces in the formation of $O_3^*/O_3 + OH$, $O_2 + O_2 + H$, and $O_2 + OH + O$. For $v < v_C$, chemical reaction occurs always with an activation energy, with reactivity increasing with translational energy.

To describe analytically the dependence of the cross section with translational energy, we have used the form

$$\sigma^x(E_{tr}, v) = \mathcal{G}(E_{tr}, v) + \mathcal{B}(E_{tr}, v) \quad (v \geq v_C, \forall E_{tr}) \quad (10)$$

$$= \mathcal{B}(E_{tr}, v) \quad (v < v_C, E_{tr} \geq E_{tr}^{th}) \quad (11)$$

$$= 0 \quad (v < v_C, E_{tr} < E_{tr}^{th}) \quad (12)$$

**TABLE 4: Energies (in kcal mol$^{-1}$) and Percentages of Energy Partitioned to Different Degrees of Freedom for the Reaction $O_2(v) + HO_2 \rightarrow O_3^*/O_3 + OH$**

| | | | | $O_3^*/O_3$ | | | | OH | | | |
|---|---|---|---|---|---|---|---|---|---|---|---|
| $v$ | $E_{tr}$ | $\langle E_{tr}\rangle$ | $\langle E_{tr}\rangle$ (%) | $\langle E_v\rangle$ | $\langle E_v\rangle$ (%) | $\langle E_r\rangle$ | $\langle E_r\rangle$ (%) | $\langle E_v\rangle$ | $\langle E_v\rangle$ (%) | $\langle E_r\rangle$ | $\langle E_r\rangle$ (%) |
| 18 | 1.0 | 7.62 | 18.9 | 21.34 | 53.0 | 9.14 | 22.7 | 1.70 | 4.2 | 0.45 | 1.1 |
| | 2.0 | 8.13 | 19.6 | 29.34 | 70.7 | 0.97 | 2.3 | 1.05 | 2.5 | 2.00 | 4.8 |
| | 4.0 | 8.18 | 18.8 | 30.19 | 69.6 | 0.39 | 1.0 | 1.69 | 3.9 | 2.95 | 6.8 |
| | 6.0 | 10.31 | 22.7 | 26.90 | 59.2 | 3.34 | 7.3 | 2.58 | 5.7 | 2.32 | 5.1 |
| | 8.0 | 9.60 | 20.3 | 27.01 | 57.0 | 5.95 | 12.6 | 2.74 | 5.8 | 2.10 | 4.4 |
| 20 | 1.0 | 8.56 | 18.3 | 27.95 | 59.9 | 3.58 | 7.7 | 2.99 | 6.4 | 3.58 | 7.7 |
| | 2.0 | 11.70 | 24.5 | 27.51 | 57.7 | 3.85 | 8.1 | 2.24 | 4.7 | 2.36 | 5.0 |
| | 4.0 | 10.92 | 22.0 | 28.62 | 57.7 | 4.93 | 9.9 | 2.42 | 4.9 | 2.69 | 5.4 |
| | 6.0 | 13.55 | 26.0 | 28.36 | 54.4 | 4.01 | 7.7 | 3.00 | 5.8 | 3.18 | 6.1 |
| | 8.0 | 13.85 | 25.9 | 30.41 | 56.9 | 4.25 | 7.9 | 2.82 | 5.3 | 2.15 | 4.0 |
| | 12.0 | 14.01 | 24.4 | 33.63 | 58.5 | 4.18 | 7.3 | 2.47 | 4.3 | 3.19 | 5.5 |
| | 16.0 | 19.03 | 31.0 | 31.71 | 51.6 | 4.31 | 7.0 | 3.75 | 6.1 | 2.63 | 4.3 |
| 24 | 1.0 | 16.85 | 29.1 | 32.33 | 55.8 | 3.31 | 5.7 | 2.60 | 4.8 | 2.85 | 4.9 |
| | 2.0 | 15.72 | 26.7 | 32.66 | 55.4 | 4.29 | 7.3 | 3.72 | 6.3 | 2.56 | 4.3 |
| | 4.0 | 16.08 | 26.4 | 34.16 | 56.2 | 4.71 | 7.7 | 2.64 | 4.3 | 3.23 | 5.3 |
| | 6.0 | 18.35 | 29.2 | 34.12 | 54.3 | 4.54 | 7.3 | 2.50 | 4.0 | 3.30 | 5.3 |
| | 8.0 | 17.89 | 27.6 | 33.85 | 52.2 | 5.98 | 9.2 | 3.14 | 4.8 | 3.93 | 6.1 |
| | 12.0 | 21.22 | 30.9 | 34.76 | 50.6 | 6.54 | 9.5 | 2.86 | 4.2 | 3.31 | 4.8 |
| 27 | 1.0 | 18.94 | 28.9 | 35.14 | 53.7 | 4.51 | 6.9 | 3.01 | 4.7 | 3.89 | 5.9 |
| | 2.0 | 19.09 | 28.7 | 35.77 | 53.8 | 5.36 | 8.1 | 3.18 | 4.8 | 3.06 | 4.6 |
| | 4.0 | 21.39 | 31.3 | 35.18 | 51.5 | 5.08 | 7.4 | 3.25 | 4.8 | 3.44 | 5.0 |
| | 6.0 | 22.29 | 31.7 | 36.52 | 52.0 | 5.03 | 7.2 | 2.84 | 4.0 | 3.58 | 5.1 |
| | 8.0 | 22.64 | 31.3 | 36.27 | 50.2 | 6.60 | 9.1 | 3.00 | 4.2 | 3.72 | 5.2 |
| | 12.0 | 25.34 | 33.3 | 36.81 | 48.4 | 6.96 | 9.2 | 3.41 | 4.5 | 3.51 | 4.6 |

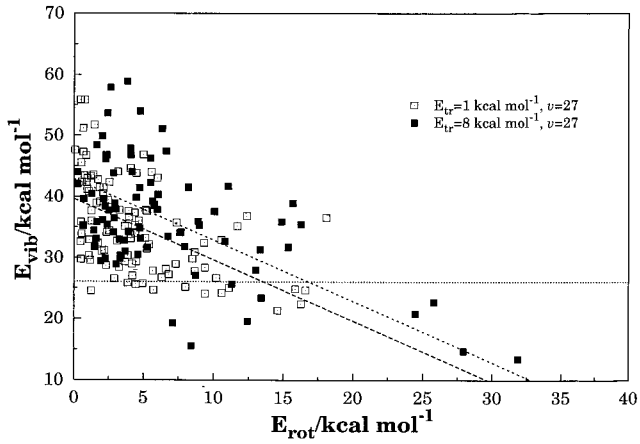


**Figure 5.** Vibrational−rotational energy distribution of products $O_3^*/O_3$. The dotted line indicates the threshold energy for dissociation into $O_2 + O$, while in dash are shown lines for the constant $E_{vib} + E_{rot}$.

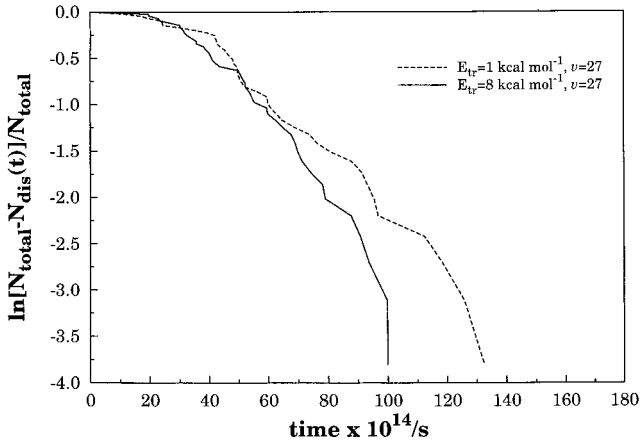


**Figure 6.** Logarithm of the decay rate of $O_3^*$ as a function time.

where the capture type contribution is defined by

$$\mathscr{C}(E_{tr}, v) = \frac{\sum_{i=1}^{n_C} c_i \Delta v^i}{E_{tr}^{n_1}} \tag{13}$$

and the barrier type term is written as

$$\mathscr{B}(E_{tr}, v) = [E_{tr} - E_{tr}^{th}(v)]^{n_2} \left(\sum_{j=0}^{n_B} d_j \Delta v^j\right) \exp[-m(E_{tr} - E_{tr}^{th}(v))] \tag{14}$$

Thus, $v_C$ is the lowest value of $v$ above which capture plays an important role. In turn, the $v$-dependent threshold energy has been found to be well-described by the form

$$E_{tr}^{th}(v) = A + b\Delta v \quad v < v_C \tag{15}$$

$$= 0 \quad v \geq v_C \tag{16}$$

where $\Delta v = v - v_{th}$ and $v_{th}$ is the threshold vibrational quantum number above which reaction can in principle take place at zero translational energy. The above model excitation function provides therefore a generalization of that employed elsewhere,[62] with the number of parameters and specific algebraic details being chosen to improve the quality of fit to the calculated data. From energetic requirements, we first fixed $v_{th} = 11$. Using this value and the calculated threshold energies, we have then determined that $v_C = 18$. In fact, eq 15 is found to fit accurately the calculated threshold energies, leading to a prediction of a zero threshold energy for $v_{th} = 18.6$, which has been rounded off to $v_C = 18$. We emphasize that the first term in eq 10 describes the $v$-dependent capture contribution of the cross section, while the second term represents the threshold energy type component. Except for $m = 0.05$, which has been kept for

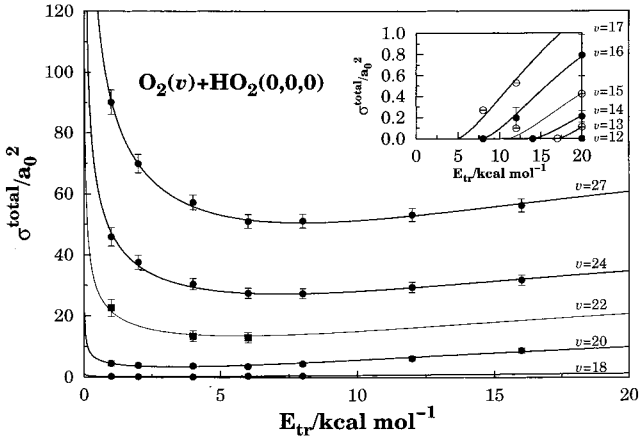


**Figure 7.** Reactive cross section $\sigma^{total}$ as a function of the translational energy for products ($O_3^*/O_3 + OH$, $O_2 + O_2 + H$, and $O_2 + OH + O$). Shown in the insert are the cross sections for $v \leq 17$. The solid symbols correspond to the calculated cross sections while the open circles have been obtained by interpolation using the former. In all cases, the rotational quantum number of $O_2$ has been fixed at $j = 1$, while the rotational energy of $HO_2$ has been assigned by using the microcanonical sampling scheme for a temperature of 300 K. Also indicated when appropriate are the 68% error bars. The model in eq 10−16, calibrated using only the solid and open circles, is also shown by the thick and thin (predicted) solid lines.

**TABLE 5: Numerical Values of Least-Squares Parameters in Eq 10−15**[a]

| parameter | $v \geq v_C$ | $v < v_C$ |
|---|---|---|
| $c_1$ | 24.8566 | nr[b] |
| $c_2$ | −8.742 19 | nr |
| $c_3$ | 1.045 40 | nr |
| $c_4$ | −4.906 94(−2)[c] | nr |
| $c_5$ | 8.246 67(−4) | nr |
| $d_0$ | −9.217 32(−1) | 8.125 42(−2) |
| $d_1$ | 2.740 08(−1) | −4.823 66(−2) |
| $d_2$ | −2.888 41(−2) | 1.118 11(−2) |
| $d_3$ | 1.428 11(−3) | −5.888 44(−4) |
| $d_4$ | −2.408 23(−5) | −1.936 23(−5) |
| $n_1$ | 0.397 506 | nr |
| $n_2$ | 1.863 13 | 1.50 |
| $m$ | 0.05 | 0.05 |
| $A$ | nr | 23.0713 |
| $b$ | nr | −3.041 66 |

[a] Units are such that with the energy in kcal mol$^{-1}$, the cross section is in $a_0^2$. [b] Not relevant. [c] Given in parentheses are the powers of 10 by which the numbers should be multiplied.

convenience from previous work,[62,63] all other parameters have been determined from a least-squares fitting procedure to the calculated data. This fit consisted of two steps. First, we have fixed $n_C = 3$ and $n_B = 2$, with the model being calibrated from a fit to the calculated cross sections for $v \geq v_C$. Using this model with a reasonably small number of parameters, we then predicted the cross sections for $v = 35$ from a fit to the data for $v = 18$, 20, 24, and 27. These were then included as guiding data with half the weight of the calculated points to determine the least-squares parameters $n_1$, $c_i$, and $d_i$ in the final model with $n_C = 5$ and $n_B = 4$. Indeed, this model containing five additional parameters was judged to be the best overall, being the optimum values of the least-squares parameters reported in Table 5 (although the standard errors can be large for the smaller coefficients, we report for the sake of reproducibility all the numbers used in our calculations). The fit was completed by using now only eq 14 to fit the data for $v < v_C$. Given the scarcity of calculated points, we provide a coverage of such low vibrational states by interpolating linearly the cross section

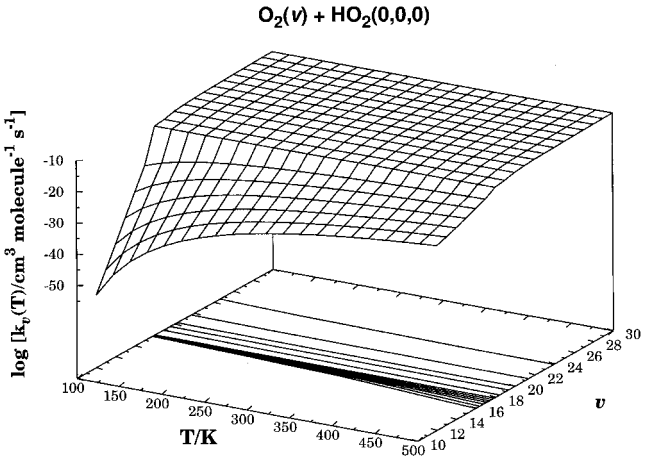


**Figure 8.** Total reactive thermal rate coefficient for $O_2(v) + HO_2$ as a function of temperature and vibrational quantum number of $O_2$.

using the two closest calculated ones for a given translational energy, e.g., $v = 14$ and 16 in the case of $v = 15$. These new points are indicated using open symbols, while the new set of numerical coefficients ($d_i$) is also given in Table 5.

Figure 7 shows the calculated cross sections for the reactive removal of $O_2(v)$, together with the model excitation function in eq 10−16. Clearly, the fitted form shows very good agreement with the calculated points and hence highlights the trends involved. It also suggests that it may be reliable in predicting the cross section for other $v$ states not specifically considered in this work, as it can be seen from the data calculated for $v = 22$ (using only $10^3$ trajectories per point), which has not been included in the least-squares fitting procedure. Of course, care must be exercised when using the above model excitation function to extrapolate far beyond the range of $v$ and $E_{tr}$ values considered in the fit (shown by the solid dots and open circles in Figure 7).

By substitution of the above model excitation function in eq 4, the specific thermal rate coefficient assumes the general form

$$k_v(T) = g_e(T)\left(\frac{8}{\pi\mu}\right)^{1/2}\left\{\left(\sum_{i=1}^{n_C} c_i \Delta v^i\right)\Gamma(2-n_1)\,(RT)^{-n_1+1/2} + \left(\sum_{j=0}^{n_B} d_j \Delta v^j\right)\frac{(RT)^{n_2+1/2}\exp[-E_{tr}^{th}(v)/RT]}{(1+mRT)^{n_2+2}} \times \left[\Gamma(n_2+2) + \Gamma(n_2+1)\,(1+mRT)E_{tr}^{th}(v)/RT\right]\right\} \quad (17)$$

where $\Gamma(...)$ is the gamma function and all other symbols have their usual meaning. For $v \geq v_C$, one has $E_{tr}^{th} = 0$ while for $v < v_C$ one must use $c_i = 0$ ($i = 1 - n_C$) with the proper value of $E_{tr}^{th}$ and corresponding set of $d_i$ coefficients (see Table 5). Following ref 62, we show in Figure 8 a perspective plot of the total reactive rate constant (i.e., for formation of products, $O_3^*/O_3 + OH$, $O_2 + O_2 + H$, and $O_2 + OH + O$) as a function of temperature and vibrational quantum number of $O_2$. The notable feature is the significant variation in the temperature dependence pattern with vibrational quantum number. While for low vibrational states ($v \geq 12$) the rate constant increases with $T$ as in a typical energy threshold regime, for high $v$ states, such a depencence is less marked or even diasppears stressing the dominant behavior of a capture type mechanism. Also observable is a somewhat sudden variation when going from $v = 17$ to 18 at a fixed temperature, which is due to the transition

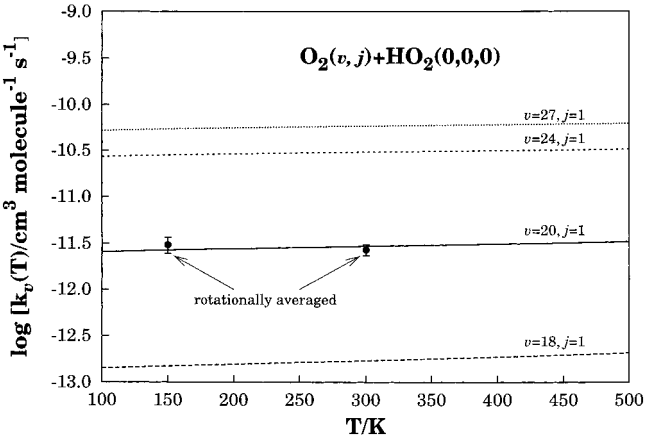


**Figure 9.** Cuts in Figure 8 for $v = 18$, 20, 24, and 27. The dots indicate the results of calculations using thermally averaged rotational distributions for $O_2$.

**TABLE 6: Calculated Specific Rate Coefficients for Formation of All Products at 298 K in cm$^3$ s$^{-1}$**

| $v$ | $k(v)$ |
|---|---|
| 18 | 1.70(−13) |
| 20 | 2.93(−12) |
| 24 | 3.04(−11) |
| 27 | 5.83(−11) |

from a pure barrier type to a mixed mechanism where capture also takes place. For completeness, Table 6 compares the calculated thermally averaged specific rate coefficients at 298 K. In turn, Figure 9 shows cuts of Figure 8 for $v = 18$, 20, 24, and 27. Clearly, the rate constants are seen to vary by almost 3 orders of magnitude when going from $v = 18$ to 27, being quite large for high $v$ states. Also shown by the dots in Figure 9 are the results obtained from rotationally averaged calculations for $v = 20$ using $2 \times 10^3$ trajectories. They suggest that the trends reported in this work for $O_2$ kept at $j = 1$ should not differ drastically from those obtained for a thermalized rotational distribution.

## 5. Conclusions

We reported a theoretical study of the title multichannel reaction, which to our knowledge, provides the first information on collisions of vibrationally excited molecular oxygen with hydroperoxyl radicals. It has been shown that the product ozone molecules are formed with a substantial amount of internal energy, both vibrational and rotational. Such molecules lead ultimately to the formation of stable ozone species via either a quenching mechanism or through dissociation followed by fast recombination of the formed oxygen atom in excess of molecular oxygen. The calculations also suggest that for $v \geq 18$, reaction occurs via both capture type and barrier type mechanisms for low and high translational energies, although reactive $O_2(v)$ removal via a capture type mechanism seems to dominate over the whole range of translational energies. No comparison with experimental data has been possible due to the unavailability of such data. We hope that the present study may stimulate work using laser techniques that allow the preparation of vibrationally hot reactant molecules.

**Acknowledgment.** The support of Fundação para a Ciência e Tecnologia, Portugal, under program PRAXIS XXI is gratefully acknowledged.

## References and Notes

(1) Hamilton, C. E.; Kinsey, J. L.; Field, R. W. *Annu. Rev. Phys. Chem.* **1986**, *37*, 493.
(2) Sepiol, J. *Chem. Phys. Lett.* **1990**, *175*, 419.
(3) Yang, X.; Kim, E. H.; Wodtke, A. M. *J. Chem. Phys.* **1990**, *93*, 4483.
(4) Ma, Z.; Jons, S. D.; Giese, C. F.; Gentry, W. R. *J. Chem. Phys.* **1991**, *94*, 8608.
(5) Zhang, Q.; Kandel, S. A.; Wasserman, T. A. W.; Vaccaro, P. H. *J. Chem. Phys.* **1992**, *96*, 1640.
(6) Price, J. M.; Mack, J. A.; Rogaski, C. A.; Wodtke, A. M. *Chem. Phys.* **1993**, *175*, 83.
(7) Yang, X.; Wodtke, A. M. *Int. Rev. Phys. Chem.* **1993**, *12*, 123.
(8) Yang, X.; Price, J. M.; Mack, J. A.; Morgan, C. G.; Rogaski, C. A.; McGuire, D.; Kim, E. H.; Wodtke, A. M. *J. Phys. Chem.* **1993**, *93*, 3944.
(9) Yang, X.; Price, J. M.; Mack, J. A.; Morgan, C. G.; Rogaski, C. A.; Wodtke, A. M. *Molecular Dynamics and Spectroscopy by Stimulated Emission Pumping*; Dai, H. L., Field, R. W., Eds.; World Scientific: Singapore, 1995; Vol. 4, p 513.
(10) Crim, F. F. *Annu. Rev. Phys. Chem.* **1984**, *35*, 657.
(11) Robinson, J. M.; Pearson, D. J.; Copeland, R. A.; Crim, F. *J. Chem. Phys.* **1985**, *82*, 780.
(12) Rensberger, K. J.; Copeland, R. A.; Robinson, J. M.; Crim, F. F. *J. Chem. Phys.* **1985**, *83*, 1132.
(13) Robinson, J. M.; Rensberger, K. J.; Crim, F. F. *J. Chem. Phys.* **1986**, *84*, 220.
(14) Rensberger, K. J.; Robinson, J. M.; Crim, F. F. *J. Chem. Phys.* **1987**, *86*, 7340.
(15) Utz, A. L.; Tobiason, J. D.; M., E. C.; Fritz, M. D.; Crim, F. F. *J. Chem. Phys.* **1992**, *97*, 389.
(16) Wu, J.; Huang, R.; Gong, M.-X.; Saury, A.; Carrasquillo, M. E. *J. Chem. Phys.* **1993**, *99*, 6474.
(17) Hartland, G. V.; Dong, Q.; Dai, H. L. *J. Chem. Phys.* **1994**, *101*, 8554.
(18) Mack, J. A.; Mikulecky, K.; Wodtke, A. M. *J. Chem. Phys.* **1996**, *105*, 4105.
(19) Parker, H.; Slanger, T. G. *J. Chem. Phys.* **1994**, *100*, 287.
(20) Miller, R. L.; Suits, A. G.; Houston, P. L.; Toumi, R.; Mack, J. A.; Wodtke, A. M. *Science* **1994**, *265*, 1831.
(21) Rogaski, C. A.; Price, J. M.; Mack, J. A.; Wodtke, A. M. *Geophys. Res. Lett.* **1993**, *20*, 2885.
(22) Houston, P. L. *Acc. Chem. Res.* **1995**, *28*, 453.
(23) Eluszkiewicz, M. A. J.; Allen, M. *J. Geophys. Res.* **1993**, *98*, 1069.
(24) Siskind, D. E.; Connor, B. J.; Remsberg, R. S. E. E. E.; Tsou, J. J.; Parrish, A. *J. Geophys. Res.* **1995**, *100*, 11191.
(25) Osterman, G. B.; Salawitch, R. J.; Sen, B.; Toon, G. C.; Stachnik, R. A.; Pickett, H. M.; Margitan, J. J.; Blavier, J.; Peterson, D. B. *Geophys. Res. Lett.* **1997**, *24*, 1107.
(26) Crutzen, P. *Science* **1997**, *277*, 1951.
(27) Varandas, A. J. C.; Wang, W. *Chem. Phys.* **1997**, *215*, 167.
(28) Wang, W.; Varandas, A. J. C. *Chem. Phys.* **1998**, *236*, 181.
(29) Varandas, A. J. C.; Pais, A. A. C. C.; Marques, J. M. C.; Wang, W. *Chem. Phys. Lett.* **1996**, *249*, 264.
(30) Garrido, J. D.; Caridade, P. J. S. B.; Varandas, A. J. C. *J. Phys. Chem. A* **1999**, *103*, 4815.
(31) Varandas, A. J. C. *Int. Rev. Phys. Chem.* **2000**, *19*, 199.
(32) Varandas, A. J. C.; Caridade, P. J. S. B. *Chem. Phys. Lett.* **2001**, *339*, 1.
(33) Caridade, P. J. S. B.; Zhang, L.; Garrido, J. D.; Varandas, A. J. C. *J. Phys. Chem. A* **2001**, *105*, 4395.
(34) Caridade, P. J. S. B.; Betancourt, M.; Garrido, J. D.; Varandas, A. J. C. *J. Phys. Chem. A* **2001**, *105*, 7435.
(35) Balakrishnan, N.; Billing, G. D. *Chem. Phys. Lett.* **1995**, *242*, 68.
(36) Balakrishnan, N.; Dalgarno, A.; Billing, G. D. *Chem. Phys. Lett.* **1998**, *288*, 657.
(37) Bates, D. R.; Nicolet, M. *J. Geophys. Res.* **1950**, *55*, 301.
(38) Hunt, B. G. *J. Geophys. Res.* **1966**, *71*, 1385.
(39) Nicolet, M. *Planet. Space Sci.* **1972**, *20*, 1671.
(40) Rowland, F. S.; Molina, M. *Rev. Geophys. Space Phys.* **1975**, *13*, 1.
(41) Nicolet, M. *Rev. Geophys. Space Phys.* **1975**, *13*, 593.
(42) Kaufman, F. *Annu. Rev. Phys. Chem.* **1979**, *30*, 411.
(43) Chang, J. S.; Duewer, W. H. *Annu. Rev. Phys. Chem.* **1979**, *30*, 443.
(44) Nicolet, M. *Adv. Chem. Phys.* **1985**, *55*, 63.
(45) Khrgian, A. K. *The Physics of Atmospheric Ozone*; Wiley: Chichester, 1975.
(46) Duewer, W. H.; Wuebbles, D. J.; Ellsaesser, H. W.; Chang, J. S. *J. Geophys. Res.* **1977**, *82*, 935.
(47) Nangia, P. S.; Benson, S. W. *J. Am. Chem. Soc.* **1980**, *102*, 3105.

(48) Paukert, T. T.; Johnston, H. S. *J. Chem. Phys.* **1972**, *56*, 2824.
(49) Poulet, G.; Bras, G. L.; Combourieu, J. *J. Chem. Phys.* **1978**, *69*, 767.
(50) Atkinson, R.; Darnall, K. R.; Lloyd, A. C.; Winer, A. M.; Pitts, J. N. J. *Adv. Photochem.* **1979**, *11*, 375.
(51) Trush, B. A. *In Pathways of Pollutants in the Atmosphere*; Royal Society: London, 1979.
(52) Leck, T. J.; Cook, E. L. J.; Birks, J. W. *J. Chem. Phys.* **1980**, *72*, 2364.
(53) Varandas, A. J. C.; Silva, J. D. *J. Chem. Soc., Faraday Trans.* **1992**, *88*, 941.
(54) Varandas, A. J. C.; Voronin, A. I. *Chem. Phys.* **1995**, *194*, 91.
(55) Pastrana, M. R.; Quintales, L. A. M.; Brandão, J.; Varandas, A. J. C. *J. Phys. Chem.* **1990**, *94*, 8073.
(56) Varandas, A. J. C.; Pais, A. A. C. C. *Mol. Phys.* **1988**, *65*, 843.
(57) Varandas, A. J. C.; Yu, H. G. *Mol. Phys.* **1997**, *91*, 301.
(58) Varandas, A. J. C.; Pais, A. A. C. C. *Theoretical and Computational Models for Organic Chemistry*; Formosinho, S., Czismadia, I., Arnaut, L., Eds.; Kluwer: Dordrecht, 1991; p 55.
(59) Varandas, A. J. C.; Zhang, L. *Chem. Phys. Lett.* **2000**, *331*, 474.
(60) Varandas, A. J. C. *Adv. Chem. Phys.* **1988**, *74*, 255.
(61) Varandas, A. J. C. In *Reaction and Molecular Dynamics*; Laganá, A., Riganelli, A., Eds.; Lecture Notes in Chemistry; Springer: Berlin, 2000; Vol. 75, p 33.
(62) Varandas, A. J. C.; Zhang, L. *Chem. Phys. Lett.* **2001**, *340*, 62.
(63) Zhang, L.; Varandas, A. J. C. *Phys. Chem. Chem. Phys.* **2001**, *3*, 1439.
(64) Atkinson, R.; Baulch, D. L.; Cox, R. A.; Hampson, R. F., Jr.; Kerr, J. A.; Troe, J. *J. Phys. Chem. Ref. Data* **1992**, *21*, 1125.
(65) Greenblatt, G. D.; Wiesenfeld, J. R. *J. Geophys. Res.* **1982**, *87*, 11145.
(66) Hase, W. L. MERCURY: a general Monte Carlo classical trajectory computer program, QCPE#453. An updated version of this code is VENUS96: Hase, W. L.; Duchovic, R. J.; Hu, X.; Komornik, A.; Lim, K. F.; Lu, D.-H.; Peslherbe, G. H.; Swamy, K. N.; van de Linde, S. R.; Varandas, A. J. C.; Wang, H.; Wolf, R. J. *QCPE Bull.* **1996**, *16*, 43.
(67) Varandas, A. J. C.; Bowman, J. M.; Gazdy, B. *Chem. Phys. Lett.* **1995**, *233*, 405.
(68) Wang, W.; González-Jonte, R.; Varandas, A. J. C. *J. Phys. Chem. A* **1998**, *102*, 6935.
(69) Marques, J. M. C.; Wang, W.; Pais, A. A. C. C.; Varandas, A. J. C. *J. Phys. Chem. A* **1996**, *100*, 17513.
(70) Varandas, A. J. C. *Faraday Discuss. Chem. Soc.* **1987**, *84*, 353.